Drying mechanism of monodisperse colloidal film: Evolution of normal stress and its correlation with microstructure

Jae Hwan Jeong, Young Ki Lee and Kyung Hyun Ahn*

School of Chemical and Biological Engineering, and Institute of Chemical Processes,
Seoul National University, Seoul 08826, Korea

* Corresponding author: ahnnet@snu.ac.kr ; +82 2 880 1897

Abstract

We investigate the drying process of monodisperse colloidal film over a wide range of Péclet number (*Pe*) by using the Brownian dynamics simulation. We analyze the detailed process in three aspects; accumulation front, normal stress, and microstructure. The evolution of particle distribution is quantified by tracking the accumulation front. The accumulated particles contribute to the continuous increase of the normal stress at the interface. At the substrate, the normal stress first stays constant and then increases as the accumulation front touches the substrate. We quantitatively analyze the stress development by a scaled normal stress difference between the two boundaries. At all tested *Pe*, the stress difference increases to the maximum, followed by a decrease during drying. Interestingly, a mismatch is observed between the stress difference maximum and the initial stress increase at the substrate. The microstructural analysis reveals that this mismatch is related to the microstructural development at the substrate.

Keywords

Brownian dynamics, colloidal film, drying, normal stress, microstructure

1. Introduction

Colloidal films are widely used in many applications, including latex painting,[1,2] paper coating,[3] catalyst,[4] filter,[5] and battery electrode.[6-8] In addition to chemical properties, structural properties, such as uniformity, microstructure, porosity, and film thickness, are of interest in these systems.[9,10] Even colloidal films with the same formulation may show different structure depending on drying conditions, e.g. evaporation rate, particle volume fraction, and temperature.[11-13] Therefore, in order to obtain the final products with desired performance, the film formation process must be fully understood.

Several experimental studies have reported the vertical structural heterogeneity in drying colloidal films. Ma *et al.* visualized the structure development during the drying process of hard latex particles (~0.5μm radius).[14] In their research, the particles were accumulated at the descending air-water interface, forming a "consolidation front".[14] Similarly, Shimmin *et al.* observed that the particle volume fraction increases at the interface, resulting in the formation of colloidal crystals in the drying of hard latex particles (~0.5μm radius).[15] Cardinal *et al.* further studied the distribution of silica particles in the drying film according to the particle size (0.1 ~ 0.5 μm radius), evaporation rate, and sedimentation rate.[16] Depending on the drying conditions, the parts were accumulated at the interface, or uniformly dispersed in the film, or deposited on the substrate.

Theoretical approaches have been developed to figure out the structural heterogeneity in drying film. As a key factor to analyze the film structure, particle volume fraction profile was carefully observed during drying.[17-21] It is well known that the particle distribution depends on the time scale of the evaporation rate, $\tau_E = H_0/\dot{E}$, and the time scale of particle diffusion, $\tau_D = H_0^2/D$ (H_0 is the initial film thickness, $\dot{E}$ is the evaporation rate, and $D = k_B T/\zeta$ is the particle diffusion coefficient). The ratio of these two time scales is quantified by the Péclet number, $Pe = \tau_D/\tau_E = H_0\dot{E}/D$. The change of volume fraction profile according to *Pe* has been studied and verified in several experimental and modeling studies.[16,22-24] In their works, the particle distribution in the film thickness direction is considered under the assumption that the influence of lateral flow is not relevant. When $Pe > 1$, the evaporation rate dominates, and the particles are accumulated at the descending interface. On the other hand, when $Pe < 1$, the particles are distributed uniformly throughout the film due to the diffusion of the particles.

Although continuum models were proven useful in predicting the particle distribution in drying film, there were limitations in observing the evolution of stress and microstructure during the drying process. Therefore, simulation studies have been adopted to figure out drying mechanisms. Reyes and Duda described the drying process of monodisperse colloidal film using the Monte Carlo simulation method.[25] The volume fraction profile was observed in the film thickness direction during drying, and particle arrangement was investigated in the final dried film. Cheng and Grest showed the influence of the evaporation rate on the particle distribution and arrangement using the molecular dynamics simulation method.[26] Most of the previous simulation studies mainly focused on the change in particle distribution according to the drying conditions.[25-28] There have been few studies on the drying mechanism in terms of the evolution of stress and microstructure. Recently, Wang and Brady observed the evolution

of the normal stress and the microstructure at the final stage using the Brownian dynamics simulation method.[29] As a result, a master curve of the normal stress was found at high Péclet number, and they explained it in terms of the convective transport in the film. However, there was a limited explanation of the correlation between the normal stress and microstructural development. Howard *et al.* intensively studied the crystallization kinetics using the molecular dynamics simulation method, but the normal stress was not investigated.[30]

In this study, inspired by the limitations of previous works, we focus on the investigation of the detailed drying mechanism of monodisperse hard-sphere colloidal film. For this purpose, we employ the Brownian dynamics simulation method to describe the drying process of colloidal film. Firstly, the evolution of the particle distribution is carefully investigated. We quantitatively analyze the particle distribution by defining an accumulation front and observing its growth during drying. Furthermore, the evolution of the normal stress is also quantitatively analyzed in terms of a scaled normal stress difference across the film. In addition, by performing a more detailed analysis of the microstructural development, we examine the direct correlation of the particle distribution, normal stress, and microstructure in the drying film.

This paper is organized as follows. Details of the simulation methods used in this work are described in Section 2. The simulation results and discussions are provided in Section 3. Finally, conclusions are given in Section 4.

2. Numerical methods

We consider the drying process of monodisperse hard-sphere colloidal films. The model

system is as follows. Hard-sphere colloidal particles with 0.5 μm radius are dispersed in a Newtonian fluid (initial volume fraction $\phi_0 = 0.1$). The initial film thickness is 30 μm, and the evaporation rate is fixed ranging from 5 - 50 μm/min (i.e. the decrease rate of the interface position). This model well describes the actual film drying process of monodisperse silica particles with the evaporation rate (approximately 2 - 80 μm/min) in air.[16]

These conditions are re-established to the three-dimensional (3D) system under the simulation platform (see Figure 1). The colloidal film is covered on a stationary planar substrate ($z = 0$). Hard-sphere particles with radius a are randomly distributed in the film with an initial particle volume fraction $\phi_0 = 0.1$ (the number of particles $N = 2{,}000$). In x- and y-directions, we set the domain size to $40a$, with periodic boundary conditions. Initial film thickness is $H_0 = 60a$, and the interface descends in the z-direction at a constant evaporation rate during drying. The simulations are conducted with the evaporation rates $\dot{E} = 0.1$, 0.5, and $1.0\,a/\tau$, which correspond to Péclet number Pe ($= \tau_D/\tau_E = H_0\dot{E}/D$) = 6, 30 and 60, respectively. Drying is continued until a final film thickness, $H = 0.18\,H_0$ is reached, where the bulk volume fraction of the film becomes to $\phi_{bulk} = 0.55$. In order to minimize the statistical errors that may occur in the simulation, all the results are averaged over 10 different initial configurations.

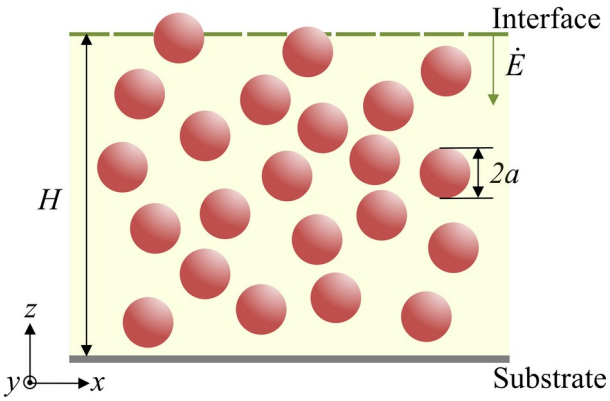

Figure 1. Schematic diagram of the monodisperse colloidal film drying.

Brownian dynamics simulation (BD) is introduced to study the colloidal film drying process.[31,32] In BD simulation, the particle motion is described by the overdamped Langevin equation.

$$\mathbf{0} = -\zeta \dot{\mathbf{r}}_i + \mathbf{f}_i^P + \mathbf{f}_i^S + \mathbf{f}_i^I + \mathbf{f}_i^B \quad (1)$$

The first term on the right-hand side of eqn (1) is the hydrodynamic force acting on the particle (Stokes friction $\zeta = 6\pi\eta a$). $\mathbf{f}_i^P$ is the force due to the interaction between particles and $\mathbf{f}_i^S$ is the force from the substrate. $\mathbf{f}_i^I$ represents the capillary force at the interface. The forces are obtained by differentiating the potentials. Here, $\mathbf{f}_i^P = -\sum_j \partial U_{ij}^P / \partial \mathbf{x}_i$ from the potential (U_{ij}^P) between the particles *i* and *j*, $\mathbf{f}_i^S = -\partial U_i^S / \partial \mathbf{x}_i$ and $\mathbf{f}_i^I = -\partial U_i^I / \partial \mathbf{x}_i$ from the particle-wall

potential (U_i^S) and particle-interface potential (U_i^I), respectively. The Brownian force $\mathbf{f}_i^B$ is generated as a random number, with zero mean and variance $\left\langle \mathbf{f}_i^B(t)\mathbf{f}_i^B(t')\right\rangle = 2\zeta k_B T\delta\left(t-t'\right)\mathbf{I}$. The above Langevin equation is numerically solved by the Euler method.[33] The (dimensionless) time step is set to be $\Delta t = 10^{-8} H_0^2/D$, which is larger than the relaxation time of the particle motion, and small enough to prevent the overlap of the particles.

The interaction of the (nearly) hard-sphere particles is modeled using the Weeks-Chandler-Andersen (WCA) type potential (96-48). In the WCA potential, an increase in the exponents changes the steepness of the potential approaching the hard-sphere potential.[34-36] We have chosen the exponents such that the normal stress measured in the simulation is comparable to the stress in the potential-free algorithm, designed to perform BD simulations on model hard spheres.[29] The potential between the particles *i* and *j* is given in the form

$$U_{ij}^P\left(r_{ij}\right) = \begin{cases} 4\varepsilon\left[\left(\dfrac{\sigma}{r_{ij}}\right)^{96} - \left(\dfrac{\sigma}{r_{ij}}\right)^{48} + \dfrac{1}{4}\right] & r_{ij} < 2^{1/48}\sigma \\ 0 & r_{ij} > 2^{1/48}\sigma \end{cases} \qquad (2)$$

where r_{ij} is the distance between the centers of the particles and $\sigma = 2a$ is the effective diameter. ε is the parameter that determines the strength of the repulsion and we set $\varepsilon = 1k_BT$.

The interaction between the particle and substrate is also described by the WCA potential (96-48)[37,38]

$$U_i^S(z_i) = \begin{cases} 4\varepsilon\left[\left(\dfrac{\sigma}{z_i + a}\right)^{96} - \left(\dfrac{\sigma}{z_i + a}\right)^{48} + \dfrac{1}{4}\right] & z_i + a < 2^{1/48}\sigma \\ 0 & z_i + a > 2^{1/48}\sigma \end{cases} \quad (3)$$

The repulsive force is applied on a particle by a virtual wall particle with the distance a from the substrate ($z = 0$) in the $-z$ direction.[37,38] Here, z_i is the height of the particle's center above the substrate.

We model the soft film interface by the purely repulsive harmonic potential.[35,39] This potential assumes a contact angle of 90º between a particle and the interface so that only the vertical capillary force is considered, neglecting the lateral capillary force.[40,41] Thus, drying simulations can be performed under the condition similar to existing studies that do not take into account the lateral flow.

$$U_i^I(z_i) = \begin{cases} 0 & z_i < H \\ \kappa(z_i - H)^2/2 & H \le z_i < H^c \\ \kappa(H^c - H)^2/2 - F^g(z_i - H^c) & z_i \quad H^c \end{cases} \quad (4)$$

where κ is a spring constant that reflects the surface tension between a particle and the interface. we take $\kappa = 1000\varepsilon/a^2$, which is large enough to move the particles along with the interface and small enough to be numerically stable.[35,42] $H^c = H + a$ is a cutoff height, where a particle completely escapes from the film and descends by the gravity F^g. The term $F^g = -\kappa(H^c - H)$ is defined to ensure that the force exerted on the particle is continuous at

$z = H^c$. In short, when the center of the particle is in $H \leq z_i < H^c$, the particle moves down by the force proportional to the distance from the interface, and it descends only by F^g when the particle completely leaves the film ($z_i \geq H^c$).

We measure the local normal stress in the z-direction. The zz component of the local normal stress, $\Sigma_{zz}(z)$, is expressed by the method of planes (MOP)[43,44]

$$\left\langle \Sigma_{zz}(z) \right\rangle = -\left\langle n(z) \right\rangle k_B T - \frac{1}{2A} \left\langle \sum_{i=1}^{N} f_{iz}^{P} \operatorname{sgn}(z_i - z) \right\rangle \quad (5)$$

where $\langle \cdot \rangle$ represents an ensemble average, $n(z)$ is the local number density of the particles, and A is the cross-sectional (x-y plane) area of the simulation box. f_{iz}^{P} is the z component of the total inter-particle forces acting on the particle i. $\operatorname{sgn}(\cdot)$ is a sign operator, which returns 1 or -1 when the input value is positive or negative, respectively. Note that the normal stress calculated from the above equation includes only the contributions of the inter-particle forces, and the forces from the substrate and interface are not considered. In addition, since the MOP method considers all the inter-particle forces, it has a clear advantage in terms of noise reduction compared to spatial binning.[43]

3. Results and discussion

First, we visually observe the distribution of particles in drying film at different Péclet

number (*Pe*). Figure 2 shows the simulation snapshots of particle configurations. In this figure, the film thickness (H) is normalized to the initial film thickness (H_0), so it decreases from 1.0 with time. When Pe = 6 (Figure 2(a)), the particles are more concentrated near the interface than in the bulk at H/H_0 = 0.8. This can be understood that the interface descends faster than the particle diffusion, leading to the accumulation of particles at the interface. And a dense particle distribution is also observed near the substrate in $H/H_0 \leq 0.6$. When Pe = 60 (Figure 2(b)), where evaporation is more dominant, the concentrated layer of particles is formed near the interface even until H/H_0 = 0.4. However, the particle distribution near the substrate does not change in $H/H_0 \geq 0.4$, and becomes denser between H/H_0 = 0.4 and 0.3.

These simulation results are similar to the experimental results of colloidal film drying for $Pe \approx 4$ and 200, respectively.[16] Cardinal *et al.* observed the cross-section of the drying film at different film thicknesses using cryo-SEM.[16] They found that the distribution of silica particles was almost uniform in the entire film at H/H_0 = 0.6 for $Pe \approx 4$. For $Pe \approx 200$, however, the particles were initially accumulated at the interface forming an ordered structure, and the accumulation region grew from the interface as drying proceeded.

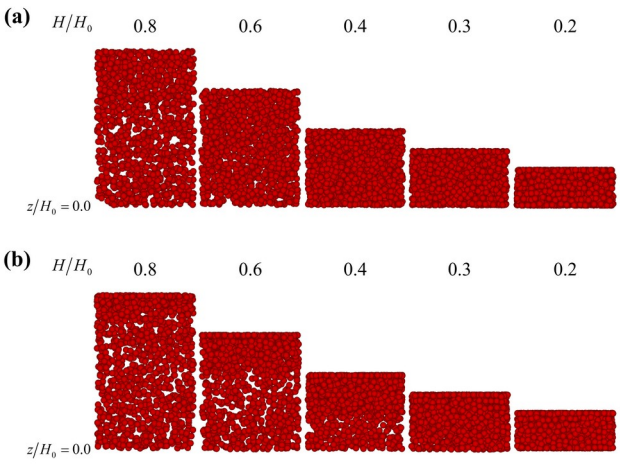

Figure 2. Time evolution of particle configuration in drying film. (a) $Pe = 6$; (b) $Pe = 60$.

Next, we quantitatively examine the changes in the particle distribution. Figure 3 shows the local volume fraction profile with the film thickness H/H_0, over the z-axis (z/H_0) of bin width $0.02a$. All the simulation results are averaged over ten different initial configurations.

Prior to full-scale analysis, we have verified our simulation results with the drying model of Wang and Brady at different Pe.[29] This model is based on the conservation equation of hard-sphere fluid expressed with a semi-empirical compressibility factor.[45] The particle distribution in the drying film was predicted by considering the collective diffusion coefficient according to the particle volume fraction.[29] When comparing the simulation results with the model prediction (Figure 3), the volume fraction profile is almost identical, except for near the two boundaries, at all Pe ($Pe = 6$ - 60) explored in the study. This means that the simulation well describes the drying mechanics of hard-sphere colloidal film. However, at the two boundaries in the simulation, the particles can exist above the interface, and cannot approach the substrate closer than the particle radius. In contrast, the boundary effects are not considered in the modeling, which induces the discrepancy between the two approaches.

We plot the local volume fraction profile at *Pe* = 6 in Figure 3(a). At H/H_0 = 0.8, the volume fraction at the interface (z/H_0 = 0.8) is about 0.2, but the volume fraction at the substrate remains the initial volume fraction of 0.1. Clearly, some particles are accumulated in the descending interface. These accumulated particles diffuse in the direction of the substrate to resolve the volume fraction gradient and form an "accumulation region".[23,35,46] In this study, we judge the position (z) in the film is included in the accumulation region if the volume fraction is higher more than 10% of the initial volume fraction i.e. $\phi(z) > 1.1\phi_0$. Below this accumulation region, there is a region that is not affected by the descending interface and maintains an initial volume fraction of 0.1, which appears in $z/H_0 < 0.4$ at H/H_0 = 0.8, for example. The accumulation region grown from the interface reaches the substrate in $H/H_0 > 0.6$, and, in turn, the volume fraction at the substrate starts to increase. As drying proceeds further, the volume fraction increases in the entire film, and its gradient formed in the vertical direction gradually decreases. At H/H_0 = 0.2, close to the final stage of drying, the volume fraction profile becomes almost uniform across the film.

When *Pe* = 30 in Figure 3(b), at H/H_0 = 0.8, the volume fraction at the interface is 0.3, slightly increased compared to the same film thickness of *Pe* = 6. The accumulation region is formed in $0.6 < z/H_0 \leq 0.8$ where a volume fraction gradient is developed. At H/H_0 = 0.6, the thickness of the accumulation region is about 0.31 H_0 which is increased by 0.08 H_0 compared to the 0.23 H_0 at H/H_0 = 0.8. In contrast to the increasing volume fraction at the

interface, the volume fraction near the substrate shows a modest change in $H/H_0 \geq 0.6$. Near the substrate, the volume fraction still maintains its initial volume fraction of 0.1 even after $H/H_0 = 0.6$, and then rapidly increases from $H/H_0 \sim 0.4$ as the accumulation region reaches the substrate. Finally, the volume fraction is comparable to that at the interface for $H/H_0 = 0.2$. When Pe = 60 (Figure 3(c)), we can confirm that the accumulation of particles is accelerated by the faster evaporation. At the same film thickness, compared to Pe = 6 and 30, the volume fraction is higher at the interface, whereas the thickness of the accumulation region is lower (0.23 H_0 at $H/H_0 = 0.6$). In addition, the film should be dried further to lower film thickness ($H/H_0 < 0.4$) for the increase in the volume fraction near the substrate.

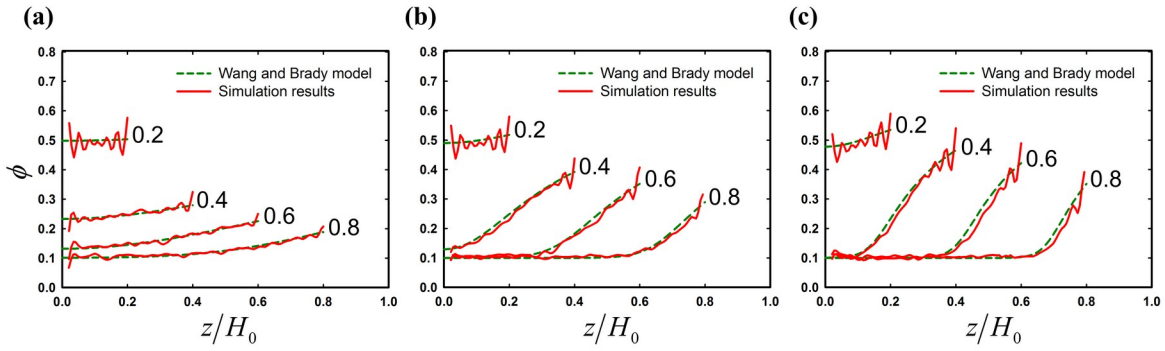

Figure 3. Local volume fraction profile with the film thickness during drying. (a) Pe = 6; (b) Pe = 30; (c) Pe = 60. The volume fraction in the model of Wang and Brady is the green dashed line, and the simulation the red solid line. H/H_0 is denoted next to the corresponding profile.

To quantify the development of the accumulation region in the drying film, the position z of the accumulation front is tracked according to the film thickness. We define the minimum value of the z-coordinates included in the accumulation region as the position of the accumulation front. In Figure 4, the evolution of the accumulation front is shown with the position of the interface (Note that the accumulation front at the initial stage in $H/H_0 > 0.96$ is not shown because it is difficult to exactly locate the accumulation front.). When comparing at the same film thickness, the gap between the interface and the accumulation front is larger at lower *Pe*. For example, at $H/H_0 = 0.8$, this distance is $0.41\,H_0$ for $Pe = 6$, $0.22\,H_0$ for $Pe = 30$, and $0.16\,H_0$ for $Pe = 60$, respectively. This result can be explained that at lower *Pe*, it takes longer time to be dried to a specific film thickness, and the particles in the accumulation region can diffuse further from the interface. Moreover, at all *Pe*, the accumulation front descends faster than the interface, and the thickness of the accumulation region increases over time. When observing at the substrate, the accumulation front reaches the substrate much earlier at lower *Pe*. The film thickness where the accumulation front contacts the substrate is $H/H_0 = 0.64$ for $Pe = 6$, $H/H_0 = 0.44$ for $Pe = 30$, and $H/H_0 = 0.33$ for $Pe = 60$, respectively.

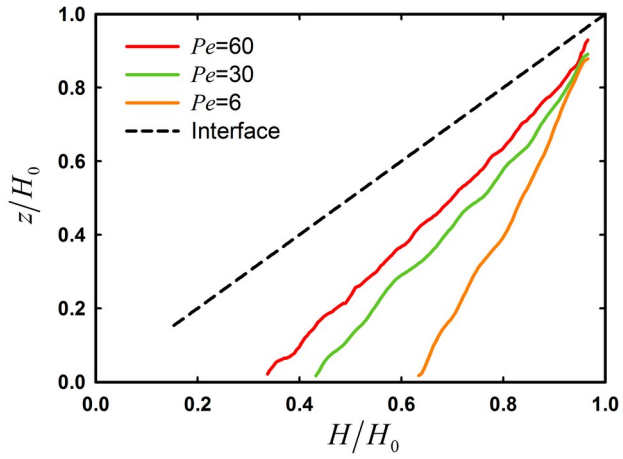

Figure 4. The position of the accumulation front with the film thickness.

Next, we investigate the local normal stress profile in drying film. This is shown in Figure 5. Note that at the initial stage, $H/H_0 > 0.96$, a large noise is generated during normal stress measurement due to insufficient particle number density at the interface. For this reason, it is not shown in the plot.

We can confirm that the local normal stress profile (Figure 5) has an almost identical pattern to the local volume fraction profile (Figure 3) for all *Pe*. This suggests that the particle volume fraction significantly contributes to the normal stress distribution. At low *Pe* (Figure 5(a)), the normal stress difference in the *z*-direction is small, indicating that the normal stress perturbation caused by the moving interface is stabilized by diffusion of particles. Consequently, the normal stress becomes uniform throughout the film. At higher *Pe*, the evaporation becomes more dominant than particle diffusion, i.e. limited time to stabilize the perturbation of normal stress, so that the normal stress difference between the interface and the substrate gradually increases over time (Figures 5(b) and (c)).[47-49] Moreover, at the same film thickness, the normal stress at the interface for *Pe* = 60 (Figure 5(c)) is higher than that

for Pe = 30 (Figure 5(b)). This can be attributed to the increased particle accumulation at the interface. Near the substrate, when Pe = 6, the normal stress shows no change until $H/H_0 \sim$ 0.6, and increases thereafter. At higher Pe, the normal stress remains at the initial value until $H/H_0 \sim 0.4$ for Pe = 30 and $H/H_0 \sim 0.3$ for Pe = 60 which is followed by a drastic increase over time.

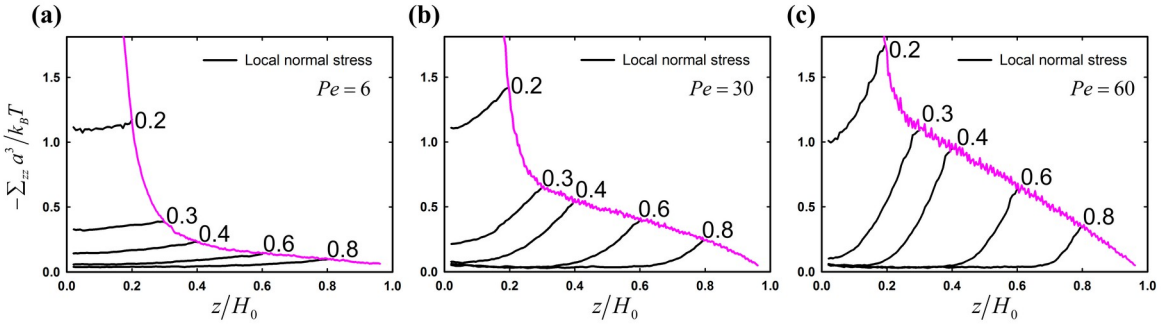

Figure 5. Local normal stress profile with the film thickness during drying. (a) Pe = 6; (b) Pe = 30; (c) Pe = 60. The black solid line represents the local normal stress profile at a given film thickness, and the pink solid line represents the normal stress at the interface over time (calculated by extrapolating to the position of the interface using the local normal stress value near the interface).

We thoroughly examine the localization of normal stress during drying. To this end, the time evolution of the normal stress is observed at the interface ($z = H$) and the substrate ($z = a$), respectively. In Figure 6(a), the normal stress at the interface increases from the beginning of drying regardless of Pe. This increase is induced by the accumulation of particles at the

interface due to the strong evaporation. On the other hand, a different stress evolution is observed at the substrate (Figure 6(b)). In the *Pe* range of this study, the normal stress at the substrate is consistent with the low initial value even when the film is dried considerably (i.e. $H/H_0 = 0.7$). The film thickness where the normal stress begins to increase is different for *Pe*, i.e. $H/H_0 = 0.63$ for $Pe = 6$, $H/H_0 = 0.42$ for $Pe = 30$, and $H/H_0 = 0.33$ for $Pe = 60$. In other words, the increase of normal stress begins at higher film thickness (early stage of drying) for lower evaporation rate. Interestingly, it is confirmed that the film thickness of the initial stress increase is very similar to the film thickness where the accumulation front starts to touch the substrate (see Figure 4). These results directly prove that the normal stress evolution is further accelerated as the accumulation front reaches the substrate.

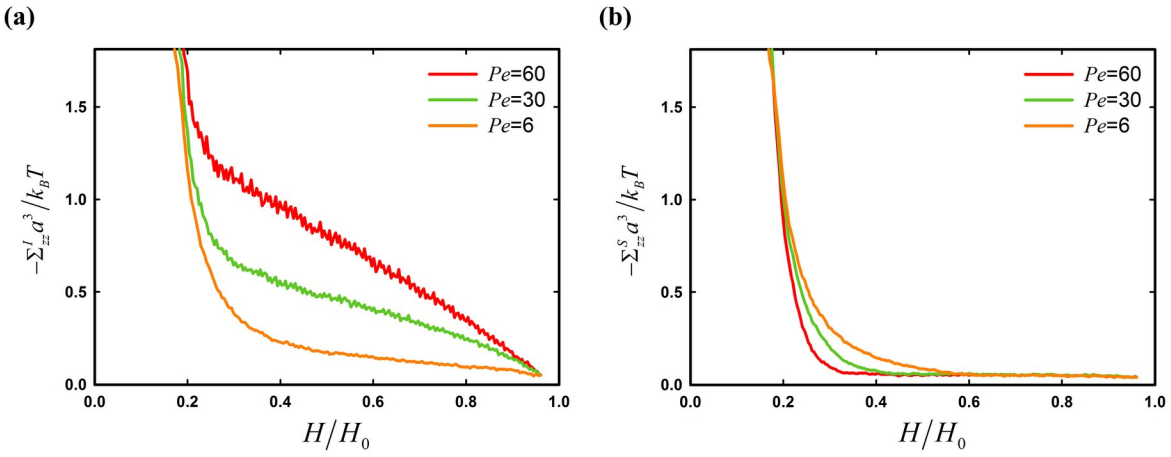

Figure 6. Development of local normal stress at the (a) interface ($z = H$) and (b) substrate ($z = a$).

Assuming one-dimensional system such that only the drying in the vertical direction (*z*-

direction) is relevant, the gradient in the *zz*-component of the normal stress is equal to the force in *z*-direction applied to the unit volume of the particle. This is the microscopic expression[50,51]

$$\partial \left\langle \Sigma_{zz}(z) \right\rangle / \partial z = \sum_{i=1}^{N} \left\langle \delta(z - z_i) f_{iz} \right\rangle \quad (6)$$

Based on the above equation, we directly observe the correlation of the normal stress difference between the interface and substrate (Figure 7) with the net motion of particles (Figure 8). Figure 7 shows the normal stress difference with the film thickness according to *Pe*. The difference is scaled by $Pen_0 k_B T$, taking into account the increased stress at the interface with the increase in *Pe* due to the localization of stress. Here, $Pen_0 k_B T = (\zeta \dot{E}/A) N$, which means the stress required to move a particle at the given evaporation rate multiplied by the total number of particles. Under this definition, the scaled normal stress difference becomes 1.0 when all the particles are affected by the falling interface.

At high *Pe*, i.e. when the particle diffusion is negligible compared to evaporation, the particles located in the region where the accumulation front just passed are accumulated and pushed down under the influence of the interface. When the interface descends by $(H_0 - H)/H_0$, the number of particles proportional to that distance is included in the accumulation region and forced to move downward. Therefore, the scaled normal stress difference is proportional to $(H_0 - H)/H_0$, and the slope becomes linear.[52,53] At *Pe* = 60, we can confirm that the slope of the curve is very close to -1 (Figure 7). In addition, larger scaled normal stress difference with decreasing *Pe* can be explained by an increase in the thickness

of the accumulation region with decreasing *Pe*. More particles in the thicker accumulation region are affected by the falling interface, which leads to an increase in the scaled normal stress difference.

For all *Pe*, the normal stress difference increases as explained above, but finally falls off after the maximum. At higher *Pe*, this maximum appears at lower film thickness. Associating with the results of Figures 4 and 6, the normal stress at the substrate maintains its initial value until the accumulation front reaches the substrate, but the normal stress at the interface increases from the beginning. Naturally, the normal stress difference, the difference between the two boundaries, increases. Likewise, when the accumulation front reaches the substrate, the normal stress near the substrate increases rapidly (see Figure 6(b)), which leads to a decrease of the normal stress difference. The maximum is observed at $H/H_0 = 0.58$ for *Pe* = 6, $H/H_0 = 0.36$ for *Pe* = 30, and $H/H_0 = 0.30$ for *Pe* = 60, respectively. It should be noted that for all *Pe*, the maximum of the normal stress difference appears at a lower film thickness than that at which the normal stress starts to increase near the substrate. Therefore, the evolution of the normal stress difference and its correlation with the microstructural change should be carefully examined for the drying stage after the accumulation front contacts the substrate.

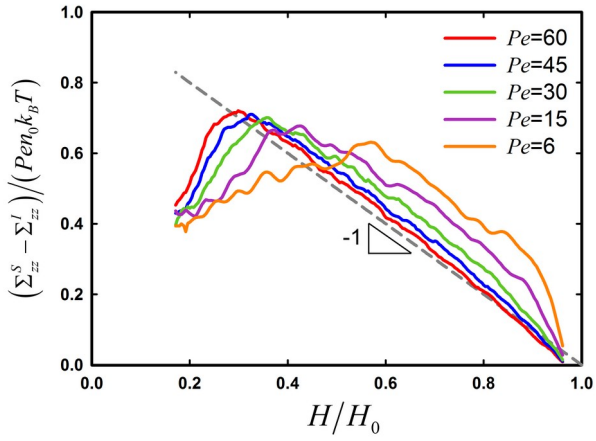

Figure 7. The scaled normal stress difference between the interface and substrate with the film thickness. The gray dotted line represents a guideline with a slope of -1.

As pointed out in eqn (6), the average velocity in the *z*-direction (vertical direction to the film surface) of all particles is computed to analyze the net motion of the particles. In Figure 8, we observe this average velocity normalized by the evaporation rate with the change of film thickness. As drying proceeds, the velocity increases for all *Pe* due to the increasing number of particles affected by the descending interface. At lower *Pe*, the normalized average velocity increases faster in the initial stage of drying. This is because not only of the particle motion induced by the interface but also of the particle diffusion toward the substrate direction induced by the volume fraction gradient. In addition, the average velocity decreases after the peak velocity at all tested *Pe*. The reason for the decrease can be explained that the downward motion of the particles is significantly hindered by the stationary substrate after the accumulation front contacts the substrate. Interestingly, the average velocity curve according to *Pe* is very similar to the scaled normal stress difference curve shown in Figure 7. This means that both the evolution of the normal stress difference and the average particle velocity in drying film can be explained by the influence of the interface and the substrate on

the particles.

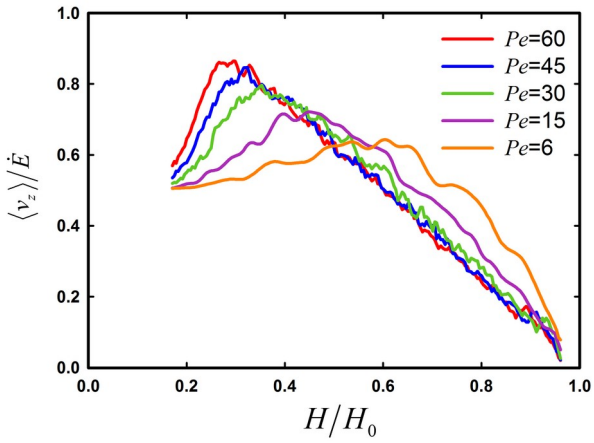

Figure 8. Normalized average particle velocity in the z-direction with the film thickness. Note that the evaporation rate has a (–) sign as the interface moves down to the $-z$ direction.

As mentioned previously, we analyze the microstructural development in drying film to examine a mismatch between the stress difference maximum and the initial stress increase at the substrate. As shown in Figure 6, the stress responses are related to the stress evolution at both the interface and substrate, so that the structural analysis needs to be carried out at both boundaries. Here, the contact number of particles at the interface ($z = H$) and substrate ($z = a$) is measured to probe the process of particle accumulation at the interface and the development of microstructure at the substrate. Especially, we focus on the microstructural change that occurs after the accumulation front reaches the substrate. For this purpose, we calculate the contact number (N_C) for all the particles located at position z ($z = H$ or a). The number of particles with each contact number is divided by the total number of particles at

that position z. Then, we can get the contact number distribution $P(z,N_C)$ (in probability function) and analyze the evolution of $P(z,N_C)$.

In Figure 9(a), $P(z,N_C)$ at the interface ($z = H$) is shown with the film thickness. At low evaporation rate $Pe = 6$, N_C shows a gradual increase with film drying. On the other hand, at higher Pe, the increase in N_C becomes more clear, because the particle accumulation at the interface is further enhanced (Figures 2 – 4).[54,55] In this case, the average of N_C increases and $P(z,N_C)$ becomes broader. Moreover, N_C shows a rapid increase at the final stage of drying, $H/H_0 \leq 0.2$, regardless of Pe. This can be explained that at higher particle volume fraction ($\phi_{bulk} \geq 0.5$), the descent of the interface leads to the compression of the film, which in turn induces a strong increase in N_C.[55]

In Figure 9(b), $P(z,N_C)$ at the substrate ($z = a$) is shown with the film thickness. At higher Pe, N_C shows a sharp increase at lower film thickness. Note that both before and after the accumulation front reaches the substrate, $P(z,N_C)$ at the substrate remains unchanged (maintains its initial value) at all Pe. Interestingly, the film thickness where N_C increases is nearly identical to the film thickness where the normal stress difference maximum appears (see Figure 7). According to these observations, we can correlate the evolution of normal stress and microstructure at the substrate. There is a regime where the contact number distribution hardly changes even though the volume fraction increases after the accumulation front reaches the substrate. Then, as the volume fraction further increases, the contact number begins to increase, which results in a significant increase of normal stress. Consequently, this contributes to the reduction of the normal stress difference.

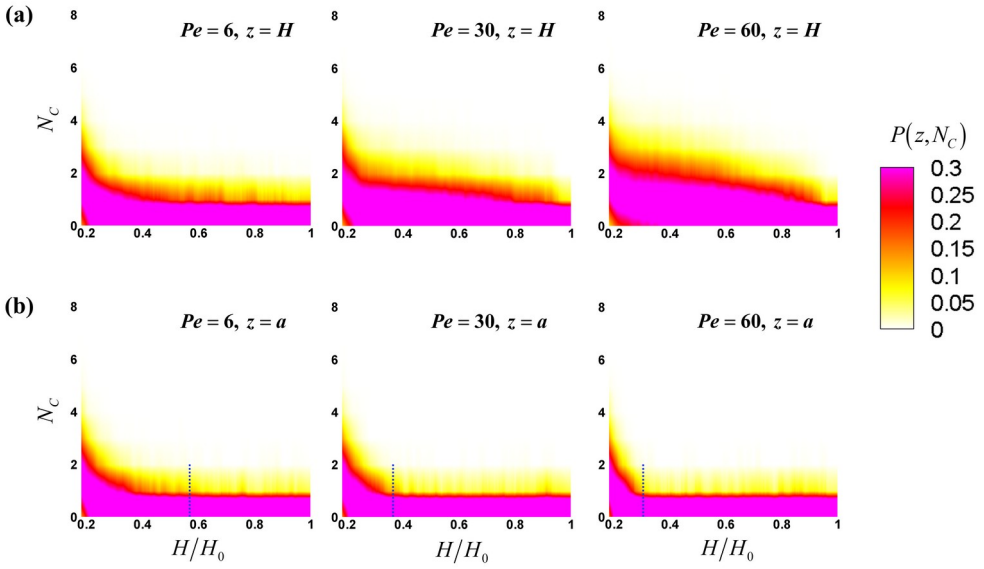

Figure 9. Average contact number distribution of particles $P(z,N_C)$ at the interface and substrate with film thickness. (a) interface ($z = H$); (b) substrate ($z = a$). The blue dotted line represents the film thickness of the normal stress difference maximum (see Figure 7).

From the above analysis, we can confirm that an increase in the particle contact number induces the local normal stress to change greatly. In the next step, to examine the microstructural change related to the contact between the particles more closely, the 2D planar pair-distribution function is computed and shown in Figure 10 (this analysis is carried out at $H/H_0 = 0.18$, where a sufficiently high contact number is observed). First, at $Pe = 6$, we observe the planar pair-distribution function in the x-y plane $g_{xy}(\mathbf{r}_{xy})$ at the interface and substrate. $g_{xy}(\mathbf{r}_{xy})$ shows an isotropic pattern at both the interface and substrate. The high magnitude peaks near $r_{xy} = 2a, 4a, 6a$ (bright pattern in Figure 10) indicate that the particles

form an ordered structure. This suggests that microstructural rearrangement can occur sufficiently in a fairly packed film due to a relatively slow evaporation rate.[56,57]

At *Pe* = 30, the peak near r_{xy} = 6a is less clear at the substrate compared to the interface, indicating that a disordered structure is formed. This can be explained with the development of the accumulation region discussed above: particle accumulation occurs at the interface, and the particles in the accumulation region move with the descending interface. The region continuously collects particles so the particle volume fraction gradually increases. Therefore, at the interface, there is enough time for the particles to rearrange in a higher volume fraction, leading to an ordered structure. On the other hand, at the substrate, the volume fraction rapidly increases after the accumulation front reaches the substrate (Figures 4 and 9). The increase of the local volume fraction occurs in too short a time for the particles to rearrange, thus leading to an increase in the contact number only (with disordered structure). For the same reason, at *Pe* = 60, the peak near r_{xy} = 6a almost disappears, and the peak near r_{xy} = 4a becomes more blurred at the substrate, indicating that a more disordered structure is formed. However, a bright ordered pattern is still observed at the interface. These results show that the structure formation at the substrate can be more sensitive to the drying conditions than that at the interface. In addition, it also means that the time for the accumulation front to contact the substrate can be a very critical factor in the formation of film structure.

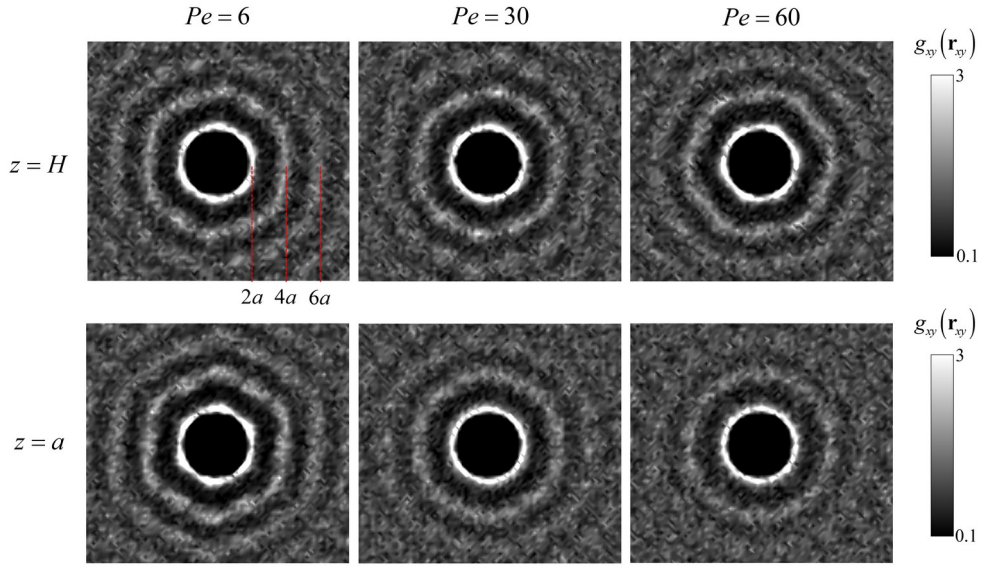

Figure 10. 2D planar pair-distribution function $g_{xy}(\mathbf{r}_{xy})$ (at $H/H_0 = 0.18$) at the interface ($z = H$) and substrate ($z = a$). Red dotted lines represent $r_{xy} = 2a$, $4a$, and $6a$ from the left, respectively.

Associating $g_{xy}(\mathbf{r}_{xy})$ with the evolution of the particle volume fraction and contact number (Figures 3, 4, 9), the structural development can be drawn as follows. For $Pe > 1$, the particles are accumulated at the descending interface, and the particle volume fraction at the interface increases (Figure 3). As the distance between particles decreases, the contact between the particles increases, and the ordering of particles begins (Figures 9 and 10). At higher Pe, the total drying time decreases so that the total time for particle rearrangement decreases. But on the other hand, the particle accumulation at the interface is strongly driven and particle rearrangement occurs from the early stage of drying. Consequently, the microstructure at the interface is influenced by these two factors (Figure 10). In contrast, near

the substrate, the volume fraction remains unchanged in the beginning. After the accumulation front reaches the substrate, the volume fraction and contact between the particles increase rapidly, and ordering begins. At higher *Pe*, the accumulation front reaches the substrate at a lower film thickness, so there is insufficient time for rearrangement to occur, resulting in a disordered structure.

Although we use an implicit solvent method that does not take into account hydrodynamic interaction, similar results can be observed in an explicit solvent method. For example, Tang *et al.* described the drying process of bi-disperse colloidal film using both the explicit and implicit solvent methods to observe the difference in the particle distribution.[58] They found that the particle distribution was almost similar in the two methods, and the hydrodynamic interaction was unimportant even at high *Pe*. In addition, Howard *et al.* studied crystallization kinetics in the drying process of monodisperse colloidal film using the molecular dynamics simulation method.[30] They reported that the hydrodynamic interaction led to an earlier onset of crystal growth, however, the final microstructure was almost identical to the case of the implicit solvent method. These results reveal that the microstructure at the final stage of drying is reasonable in our simulation though hydrodynamic interaction is not considered. The microstructure at the substrate is, however, still unveiled for both the implicit and explicit solvent methods, so that an appropriate study needs to be achieved in the future.

4. Conclusions

We investigated the evolution of the normal stress and microstructure in the monodisperse hard-sphere colloidal film drying process by using the Brownian dynamics simulation

method. When $Pe > 1$, the evaporation rate is dominant, and the particles are accumulated at the evaporating interface and the accumulation region grows. The development of the accumulation region is quantified by tracking the accumulation front. The distance between the accumulation front and the interface is larger at lower Pe at the same film thickness, leading to the accumulation front reaching the substrate much earlier. These accumulated particles localize the stress at the interface, which induces continuous increase of the stress from the beginning of the drying process. At the substrate, the normal stress first maintains the initial value and then increases with the accumulation front touching the substrate. The influence of the evaporating interface and stationary substrate on the stress development has been quantified by the scaled normal stress difference between the two boundaries. Before the accumulation front reaches the substrate, the scaled normal stress difference increases with time due to the normal stress increase at the interface. At higher Pe ($Pe = 60$), all the particles in the region where the accumulation front passed are accumulated and forced to move down with the interface, and accordingly, the scaled normal stress difference increases with the slope of -1. As Pe decreases, more particles are affected by the interface at the same film thickness, so that the initial scaled normal stress difference is higher. At all Pe discussed in this study ($Pe = 6$ - 60), the scaled normal stress difference increases to the maximum, followed by the decrease in the final stage. Interestingly, a mismatch is observed between the stress difference maximum and the initial stress increase at the substrate. This mismatch is explained by the contact number distribution of the particles. At the substrate, the contact number distribution remains unchanged even though the accumulation front reaches the substrate, and then increases as the particle volume fraction further increases. We found that the increase of contact between the particles results in a significant increase of the normal stress, which leads to the decrease in the scaled normal stress difference. In addition, the formation of the accumulation region influences the final structure of the film. As the

accumulation front contacts the substrate at low film thickness, the disordered structure is formed due to the limited time for particle rearrangement. So the structure formation at the substrate is more sensitive to *Pe* than that at the interface. This correlation of the particle distribution during drying with the evolution of the normal stress and microstructure is believed to provide insights into the drying process of the monodisperse hard-sphere colloidal film.

Conflicts of interest

There are no conflicts of interest to declare.

Acknowledgement

This work was supported by a National Research Foundation of Korea (NRF) grant funded by the Korea government (MSIT) (No. 2018R1A5A1024127).

References

1. Keddie J, Routh AF. *Fundamentals of latex film formation: processes and properties*: Springer Science & Business Media; 2010.

2. Luo H, Cardinal CM, Scriven L, Francis LF. Ceramic nanoparticle/monodisperse

latex coatings. *Langmuir.* 2008;24(10):5552-5561.

3. Järnström J, Ihalainen P, Backfolk K, Peltonen J. Roughness of pigment coatings and its influence on gloss. *Applied Surface Science.* 2008;254(18):5741-5749.

4. Hou J, Yang M, Ke C, et al. Platinum-group-metal catalysts for proton exchange membrane fuel cells: From catalyst design to electrode structure optimization. *EnergyChem.* 2020;2(1):100023.

5. Barg S, Innocentini MD, Meloni RV, et al. Physical and high-temperature permeation features of double-layered cellular filtering membranes prepared via freeze casting of emulsified powder suspensions. *Journal of membrane science.* 2011;383(1-2):35-43.

6. Lim S, Kim S, Ahn KH, Lee SJ. Stress development of Li-ion battery anode slurries during the drying process. *Industrial & Engineering Chemistry Research.* 2015;54(23):6146-6155.

7. Stein IV M, Mistry A, Mukherjee PP. Mechanistic understanding of the role of evaporation in electrode processing. *Journal of The Electrochemical Society.* 2017;164(7):A1616.

8. Nulu A, Nulu V, Sohn KY. Silicon and porous MWCNT composite as high capacity anode for lithium-ion batteries. *Korean Journal of Chemical Engineering.* 2020;37(10):1795-1802.

9. Brewer DD, Shibuta T, Francis L, Kumar S, Tsapatsis M. Coating process regimes in particulate film production by forced-convection-assisted drag-out. *Langmuir.* 2011;27(18):11660-11670.

10. Velev OD, Gupta S. Materials Fabricated by Micro−and Nanoparticle Assembly–The Challenging Path from Science to Engineering. *Advanced Materials.* 2009;21(19):1897-1905.

11. Keddie JL. Film formation of latex. *Materials Science and Engineering: R: Reports.*

1997;21(3):101-170.

12. Kim S, Sung JH, Lim S, Ahn KH. A generality in stress development of silica/poly (vinyl alcohol) mixtures during drying process. *Progress in Organic Coatings.* 2015;88:304-309.

13. Lee J, Sung S, Kim Y, Park JD, Ahn KH. A new paradigm of materials processing—heterogeneity control. *Current opinion in chemical engineering.* 2017;16:16-22.

14. Ma Y, Davis H, Scriven L. Microstructure development in drying latex coatings. *Progress in Organic Coatings*. 2005;52(1):46-62.

15. Shimmin RG, DiMauro AJ, Braun PV. Slow Vertical Deposition of Colloidal Crystals: A Langmuir− Blodgett Process? *Langmuir.* 2006;22(15):6507-6513.

16. Cardinal CM, Jung YD, Ahn KH, Francis L. Drying regime maps for particulate coatings. *AIChE journal.* 2010;56(11):2769-2780.

17. Brown L, Zukoski C, White L. Consolidation during drying of aggregated suspensions. *AIChE journal.* 2002;48(3):492-502.

18. Routh AF, Zimmerman WB. Distribution of particles during solvent evaporation from films. *Chemical Engineering Science.* 2004;59(14):2961-2968.

19. Narita T, Hebraud P, Lequeux F. Effects of the rate of evaporation and film thickness on nonuniform drying of film-forming concentrated colloidal suspensions. *The European Physical Journal E.* 2005;17(1):69-76.

20. Trueman R, Domingues EL, Emmett S, Murray M, Routh A. Auto-stratification in drying colloidal dispersions: A diffusive model. *Journal of colloid and interface science.* 2012;377(1):207-212.

21. Schulz M, Keddie J. A critical and quantitative review of the stratification of particles during the drying of colloidal films. *Soft matter.* 2018;14(30):6181-6197.

22. Im SH, Park OO. Effect of evaporation temperature on the quality of colloidal crystals

at the water− air interface. *Langmuir.* 2002;18(25):9642-9646.

23. Ekanayake P, McDonald P, Keddie J. An experimental test of the scaling prediction for the spatial distribution of water during the drying of colloidal films. *The European Physical Journal Special Topics.* 2009;166(1):21-27.

24. Trueman R, Lago Domingues E, Emmett S, Murray M, Keddie J, Routh A. Autostratification in drying colloidal dispersions: experimental investigations. *Langmuir.* 2012;28(7):3420-3428.

25. Reyes Y, Duda Y. Modeling of drying in films of colloidal particles. *Langmuir.* 2005;21(15):7057-7060.

26. Cheng S, Grest GS. Molecular dynamics simulations of evaporation-induced nanoparticle assembly. *The Journal of chemical physics.* 2013;138(6):064701.

27. Fujita M, Yamaguchi Y. Multiscale simulation method for self-organization of nanoparticles in dense suspension. *Journal of Computational Physics.* 2007;223(1):108-120.

28. Chun B, Yoo T, Jung HW. Temporal evolution of concentration and microstructure of colloidal films during vertical drying: a lattice Boltzmann simulation study. *Soft Matter.* 2020;16(2):523-533.

29. Wang M, Brady JF. Microstructures and mechanics in the colloidal film drying process. *Soft Matter.* 2017;13(44):8156-8170.

30. Howard MP, Reinhart WF, Sanyal T, Shell MS, Nikoubashman A, Panagiotopoulos AZ. Evaporation-induced assembly of colloidal crystals. *The Journal of chemical physics.* 2018;149(9):094901.

31. Heyes D, Melrose J. Brownian dynamics simulations of model hard-sphere suspensions. *Journal of non-newtonian fluid mechanics.* 1993;46(1):1-28.

32. Foss DR, Brady JF. Brownian dynamics simulation of hard-sphere colloidal

dispersions. *Journal of Rheology.* 2000;44(3):629-651.

33. Allen MP, Tildesley DJ. *Computer simulation of liquids*: Oxford university press; 2017.

34. Weeks JD, Chandler D, Andersen HC. Role of repulsive forces in determining the equilibrium structure of simple liquids. *The Journal of chemical physics.* 1971;54(12):5237-5247.

35. Howard MP, Nikoubashman A, Panagiotopoulos AZ. Stratification dynamics in drying colloidal mixtures. *Langmuir.* 2017;33(15):3685-3693.

36. Jover J, Haslam A, Galindo A, Jackson G, Müller E. Pseudo hard-sphere potential for use in continuous molecular-dynamics simulation of spherical and chain molecules. *The Journal of Chemical Physics.* 2012;137(14):144505.

37. Deb D, Winkler A, Yamani MH, Oettel M, Virnau P, Binder K. Hard sphere fluids at a soft repulsive wall: A comparative study using Monte Carlo and density functional methods. *The Journal of chemical physics.* 2011;134(21):214706.

38. Telezki V, Klumpp S. Simulations of structure formation by confined dipolar active particles. *Soft Matter.* 2020.

39. Fortini A, Martín-Fabiani I, De La Haye JL, et al. Dynamic stratification in drying films of colloidal mixtures. *Physical review letters.* 2016;116(11):118301.

40. Pieranski P. Two-dimensional interfacial colloidal crystals. *Physical Review Letters.* 1980;45(7):569.

41. Velev OD, Denkov ND, Paunov VN, Kralchevsky PA, Nagayama K. Direct measurement of lateral capillary forces. *Langmuir.* 1993;9(12):3702-3709.

42. Fortini A, Sear RP. Stratification and size segregation of ternary and polydisperse colloidal suspensions during drying. *Langmuir.* 2017;33(19):4796-4805.

43. Todd B, Evans DJ, Daivis PJ. Pressure tensor for inhomogeneous fluids. *Physical*

Review E. 1995;52(2):1627.

44. Heyes D, Smith E, Dini D, Zaki T. The equivalence between volume averaging and method of planes definitions of the pressure tensor at a plane. *The Journal of chemical physics.* 2011;135(2):024512.

45. Mulero Á. *Theory and simulation of hard-sphere fluids and related systems.* Vol 753: Springer; 2008.

46. Inasawa S, Oshimi Y, Kamiya H. Formation kinetics of particulate films in directional drying of a colloidal suspension. *Soft matter.* 2016;12(32):6851-6857.

47. Schall P, Weitz DA, Spaepen F. Structural rearrangements that govern flow in colloidal glasses. *Science.* 2007;318(5858):1895-1899.

48. Hartkamp R, Ghosh A, Weinhart T, Luding S. A study of the anisotropy of stress in a fluid confined in a nanochannel. *The Journal of chemical physics.* 2012;137(4):044711.

49. Colombo J, Del Gado E. Stress localization, stiffening, and yielding in a model colloidal gel. *Journal of rheology.* 2014;58(5):1089-1116.

50. Dhont JK, Briels WJ. Rod-like Brownian particles in shear flow. *Soft Matter: Complex Colloidal Suspensions, edited by G. Gompper, M. Schick.* 2004;2.

51. Brady JF. Particle motion driven by solute gradients with application to autonomous motion: continuum and colloidal perspectives. *Journal of Fluid Mechanics.* 2011;667:216-259.

52. Sear RP, Warren PB. Diffusiophoresis in nonadsorbing polymer solutions: The Asakura-Oosawa model and stratification in drying films. *Physical Review E.* 2017;96(6):062602.

53. Sear RP. Stratification of mixtures in evaporating liquid films occurs only for a range of volume fractions of the smaller component. *The Journal of chemical physics.*

2018;148(13):134909.

54. Whitmer JK, Luijten E. Sedimentation of aggregating colloids. *The Journal of Chemical Physics.* 2011;134(3):034510.

55. Kaewpetch T, Gilchrist JF. Chemical vs. mechanical microstructure evolution in drying colloid and polymer coatings. *Scientific reports.* 2020;10(1):1-10.

56. Rahmani Y, Van Der Vaart K, Van Dam B, Hu Z, Chikkadi V, Schall P. Dynamic heterogeneity in hard and soft sphere colloidal glasses. *Soft Matter.* 2012;8(15):4264-4270.

57. Hunter GL, Weeks ER. The physics of the colloidal glass transition. *Reports on progress in physics.* 2012;75(6):066501.

58. Tang Y, Grest GS, Cheng S. Stratification of drying particle suspensions: Comparison of implicit and explicit solvent simulations. *The Journal of chemical physics.* 2019;150(22):224901.